


RESEARCH ARTICLE | MARCH 28 2023

Correlative microscopy and monitoring of segregation processes in optoelectronic semiconductor materials and devices

Daniel Abou-Ras ; Ulrike Bloeck; Sebastián Caicedo-Dávila; ... et. al

 Check for updates

Journal of Applied Physics 133, 121101 (2023)

<https://doi.org/10.1063/5.0138952>


View
Online


Export
Citation

 CrossMark

Articles You May Be Interested In

Halide ion migration in lead-free all-inorganic cesium tin perovskites

Appl. Phys. Lett. (July 2021)

Epitaxial mid-IR nanophotonic optoelectronics

Appl. Phys. Lett. (May 2022)

Optoelectronic intelligence

Appl. Phys. Lett. (April 2021)



Time to get excited.
Lock-in Amplifiers – from DC to 8.5 GHz

[Find out more](#)

 Zurich
Instruments

Correlative microscopy and monitoring of segregation processes in optoelectronic semiconductor materials and devices

Cite as: J. Appl. Phys. **133**, 121101 (2023); doi: [10.1063/5.0138952](https://doi.org/10.1063/5.0138952)

Submitted: 16 December 2022 · Accepted: 8 March 2023 ·

Published Online: 28 March 2023



Daniel Abou-Ras,^{1,a)} Ulrike Bloeck,¹ Sebastián Caicedo-Dávila,^{1,b)} Alberto Eljarrat,² Hannah Funk,¹ Adnan Hammud,³ Sinju Thomas,¹ Dan R. Wargulski,¹ Thomas Lunkenbein,³ and Christoph T. Koch²

AFFILIATIONS

¹Helmholtz Zentrum Berlin für Materialien und Energie GmbH, Hahn-Meitner-Platz 1, 14109 Berlin, Germany

²Humboldt-Universität zu Berlin, Institut für Physik, Newtonstraße 15, 12489 Berlin, Germany

³Department of Inorganic Chemistry, Fritz-Haber-Institut der Max-Planck-Gesellschaft, Faradayweg 4–6, 14195 Berlin, Germany

^{a)}Author to whom correspondence should be addressed: daniel.abou-ras@helmholtz-berlin.de

^{b)}Now at: Department of Physics, Technical University of Munich, 85748 Garching, Germany.

ABSTRACT

The present work comprises a practical tutorial on the topic of correlative microscopy and its application to optoelectronic semiconductor materials and devices. For the assessment of microscopic structure–property relationships, correlative electron microscopy, combined also with scanning-probe and light microscopy, exhibits a collection of indispensable tools to analyze various material and device properties. This Tutorial describes not only the various microscopy methods but also the specimen preparation in detail. Moreover, it is shown that electron microscopy can serve to monitor phase segregation processes on various length scales in semiconductor nanoparticles and thin films. Algorithms used to extract phase information from high-resolution transmission electron micrographs are explained.

Published under an exclusive license by AIP Publishing. <https://doi.org/10.1063/5.0138952>

I. INTRODUCTION

Optoelectronic semiconductor devices, such as solar cells or light-emitting diodes, consist typically of several functional layers whose material properties have an impact on the performance of the complete device. It is of great importance for the research and development of these devices to understand well the link between the materials properties, including the interfaces between functional layers, and the device performance. Since very often the spatial dimensions of functional layers are on the submicrometer length scale, microscopic analyses need to be employed to characterize the corresponding structure–property relationships in optoelectronic semiconductor devices.

In order to assess these relationships, the link between microstructure (in polycrystalline materials, i.e., grain sizes, local orientations, extended structural defects such as grain boundaries, stacking faults, and dislocations), as well as elemental or phase distributions on one hand and the electrical as well as optoelectronic properties on the other hand need to be highlighted by corresponding,

microscopic measurements. Ultimately, it is of interest to determine the influence of the microscopic materials properties on the macroscopic device performance.

For the assessment of structure–property relationships, correlative electron microscopy offers a versatile toolbox, consisting of various methods necessary to characterize various materials properties. In the first part of the present Tutorial paper, we give an overview of these electron microscopy techniques, using thin-film solar cells as exemplary devices, and highlight the need to apply these techniques in a correlative manner, i.e., if possible, on identical acquisition areas. We also describe possible measurement configurations as well as the corresponding specimen-preparation routines for the electron microscopy analyses. The second part of the present work deals with phase segregation processes in semiconductor thin films and nanoparticles as well as with their monitoring by means of electron microscopy. We intend to provide a practical Tutorial to all readers who would like to apply the described approaches to various materials systems and devices. Regarding the vast literature on

various combinational microscopy works, a complete review covering all of the possible correlative analyses applied to optoelectronic semiconductor materials and devices cannot be expected. We selected the techniques discussed in the present work corresponding to our expertise and to our own research work.

II. CORRELATIVE ELECTRON MICROSCOPY

A. Definition of the term and objective

It is convenient to define the term “correlative electron microscopy” used throughout the present work, especially since in different research communities (e.g., life science vs material science), this term has also different meanings, and the corresponding approach is applied with different purposes. Since we are dealing with optoelectronic semiconductor devices, correlative electron microscopy refers to characterizing microstructural, compositional, electrical, and optoelectronic properties of functional materials and to correlating these properties with respect to their influence on the device performance. It is advantageous for this approach to conduct all analyses on the identical acquisition areas, even though in some cases, multiple analyses on an identical position are not possible owing to substantial electron-beam sensitivity of the analyzed materials. It is important to point out that the obtained microscopic structure–property relationships together with the various materials properties are important input parameters for two-dimensional or three-dimensional models of the corresponding devices.

B. Importance of specimen preparation

Before even considering specific analyses, it is essential to prepare corresponding specimens from materials or devices. Basically, specimen preparation for electron microscopy is all about optimizing the analyzed surfaces in terms of roughness or contamination. We note that for scanning electron microscopy (SEM), there is one surface (in reflection configuration), and for transmission electron microscopy (TEM), there are two surfaces to be optimized (electrons transmitted through a thin lamella). Roughnesses

or contamination on these surfaces (as well as the lamella thickness of electron-transparent specimens) may introduce artifacts in the microscopic results, which complicate their correct interpretation and evaluation. Since plan-view analyses do not require substantial preparation of surfaces, we will provide corresponding details directly in the descriptions of these analyses and will focus in Secs. II B 1 and II B 2 on procedures for cross-sectional specimen preparation.

1. Cross-sectional preparation using mechanical and Ar-ion polishing

Thin-film solar cells used as exemplary optoelectronic semiconductor devices in the present Tutorial consist of layer stacks deposited on rigid (glass) or flexible substrates (metal or polymer foils). Whenever wide specimen areas (0.1–1 mm, orders of magnitude) need to be analyzed in cross-sectional configuration, e.g., in case that good statistics of materials properties are required, preparation via combined mechanical and Ar-ion polishing is recommended. Since this preparation routine involves the use of water, the materials under investigation must not only be not water soluble but also must be inert against water. Although similar preparation procedures have been described in the literature (e.g., Ref. 1), we decided to still give a full account of our own preparation recipe here, since it contains some special steps not described elsewhere. We focus in the following on specimen preparation for SEM analyses but note that a similar procedure can be applied when preparing specimens transparent for the electron beam.

The samples are sawn into pieces of $3\text{--}4 \times 4\text{--}5 \text{ mm}^2$ in size and glued face to face together by means of an epoxy resin. For EBIC analyses (see below), one of the two sample pieces is sawn slightly longer (8–10 mm) in order to provide areas for contacting.² These sandwiched stacks are then glued edge-on to an aluminum stub. For the next step, it is convenient to cut off parts of the stub parallel to the glue line [see Fig. 1(a)]. A roof is ground using rough SiC sandpaper in such a way that the glue line resides on the crest of the roof [Figs. 1(a) and 1(b)]. This step results in a very

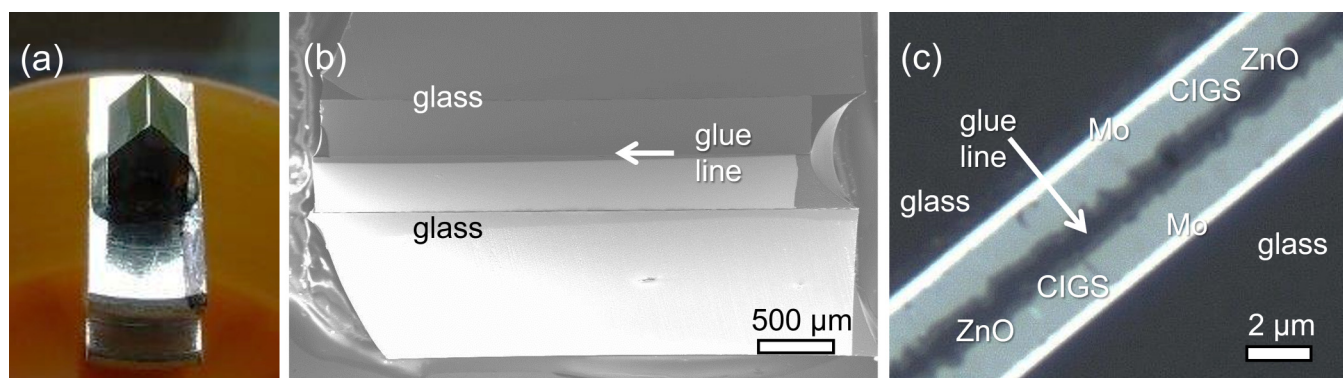


FIG. 1. (a) Photograph of two solar-cell stacks on glass, glued together face-to-face using an epoxy glue. The crest of the roof-shaped top part contains the glue line with the adjacent solar-cell stacks. (b) Scanning electron micrograph of the crest region of the specimen. (c) Optical micrograph of the ZnO/CdS/Cu(In,Ga)Se₂ (CIGS)/Mo/glass solar-cell stacks glued together face-to-face.

small area on the crest that is polished subsequently using a 1- μm diamond abrasive foil. The advantage of this approach is that only a few turns on a rotating polishing table are needed, thus, mechanical damages of the material are minimized. The final, mechanical polishing is performed using a 50-nm Al_2O_3 grinding disk until the layer stacks of both solar cells are visible clearly in an optical microscope [Fig. 1(c)].

Subsequently, the cross-sectional surface is polished using an Ar-ion beam etching system at 3 kV, 1 mA, and incident angles of 4° – 7° for about 10–20 min. In order to avoid contamination and also charging during the SEM analyses, a carbon layer (nominally about 6 nm) is deposited on the cross-sectional surface. From our experience, specimen surfaces can be conserved during several months and even years by such a carbon layer, e.g., for electron backscatter diffraction (EBSD) analyses (see below).

2. Cross-sectional preparation using focused-ion beam

Whenever a specimen is to be prepared from a specific site on a thin-film solar cell, it is convenient to use focused-ion beam (FIB) instruments.^{3–5} In the following, the preparation procedure for TEM lamellae is described; we note that a similar approach can be used for specimens analyzed by SEM techniques or also those for atom-probe tomography (APT).

Figure 2 depicts details on the FIB preparation of a TEM lamella from a tandem solar cell made of a silicon bottom cell and a halide-perovskite-type (HaP) top cell (for more information about these devices, the reader is referred to Ref. 6) The TEM lamella preparation of HaP solar-cell devices by focused-ion beam is a good example of material systems for which special care has to be taken, with respect to potential artifacts and sample sensitivity to the ion beam on the one hand, as well as to the electron beam used for imaging of the specimen during the preparation on the other hand.^{7–11} In view of the tandem solar cell (as also other

thin-film solar cells) being made of a thin-film stack, an upside-down preparation procedure¹² is preferred.

To protect the sample surface from beam damages during the milling process, two protection layers are deposited by means of electron-beam-induced and ion-beam-induced platinum deposition before initiating the actual ion-milling process. Then, trenches are formed on two neighboring positions on the site of interest via FIB milling, leaving a strip in between these positions. This strip becomes the TEM lamella via continuous enlarging of the trenches.

At a thickness of about 1 μm , the lamella is lifted out and fixed upside-down on the TEM grid in order to perform the milling process from the Si bulk towards the solar-cell surface [Fig. 2(a)]. This procedure ensures more homogenous milling and sputter rates and inhibits curtaining artifacts and potential overlapping of the stack by platinum nanoparticles originating from the deposited platinum layers.

Taking into account the redeposition dynamics during ion-milling processes as well as the fact that the main redeposition of removed material occurs underneath the ion-beam incidence point at low incidence angles, a top-down scan direction is performed, i.e., from the bulk to the surface, in order to simultaneously remove material potentially redeposited on the cross-sectional surface.

For the rough thinning of the lamella, the ion energy is decreased to 16 keV, and ion-beam currents of 10–100 pA (orders of magnitude) are applied until a lamella thickness of about 200 nm is reached. This rough thinning is followed by a low-energy milling step at 5 keV down to a thickness of about 100 nm. Finally, a cleaning and polishing step at 2 keV is performed, until reaching the final thickness of about 30 nm [Fig. 2(b)]. This succession of preparation steps aims at minimizing material damage as well as Ga implantation into the lamella sidewalls.³ For SEM imaging during the FIB milling, low beam energies as well as low electron-beam currents (e.g., 2 keV and 25 pA) are preferred, also in order to reduce beam damage to a minimum.

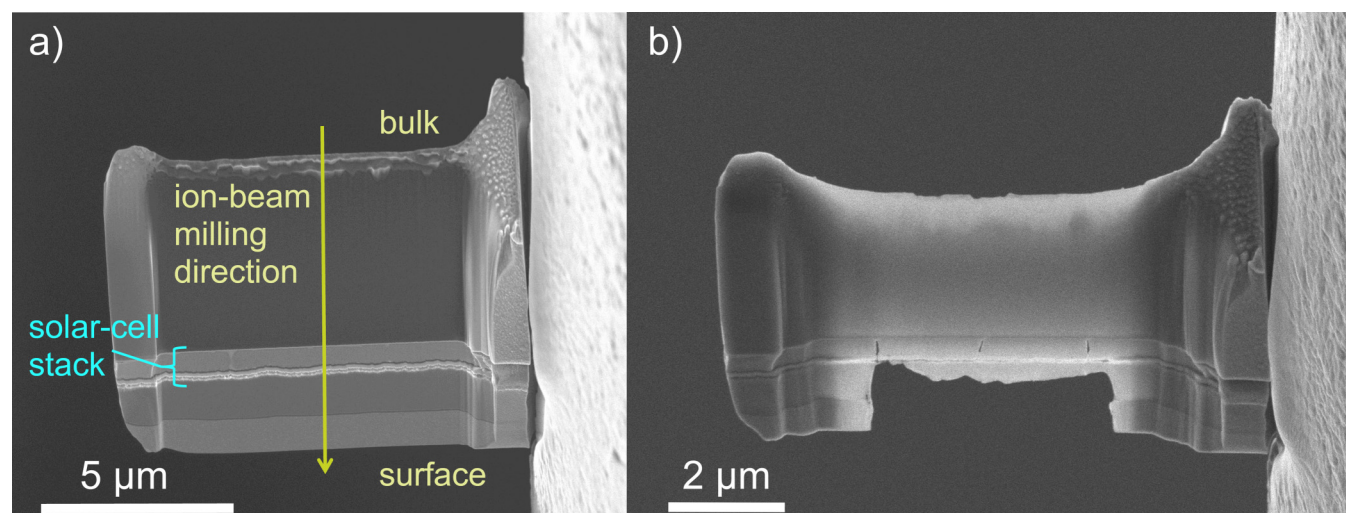


FIG. 2. (a) SEM image of a lamella of a HaP/Si tandem solar cell, showing the upside-down technique. (b) SEM image depicting the final lamella.

We would like to note that ion-beam milling is generally not a congruent process. This is, the sputtering rates (that depend on several material properties, not discussed in detail here) may be different for the different matrix elements in a sputtered compound, depending on their individual partial pressures.¹³ In this case, some matrix elements are sputtered at higher rates than others, leading to the formation of agglomerates made of the remaining elements. By using low beam energies, very low temperatures during FIB milling, or by reactive gases forming volatile compounds with the remaining elements, it is possible to impede the agglomerate formation.¹³

C. Electron microscopy techniques

In Secs. II C 1–II C 5, we describe briefly the electron microscopy methods that were used for the results given in the present Tutorial paper. We note that more extensive overviews are available in the literature (e.g., Ref. 14).

1. Imaging

Acquiring images of a specimen seems to be always the simplest part of all analyses, but can be rather demanding, especially if specific contrasts are to be obtained. A good overview of various imaging modes in TEM can be found in Ref. 15. One can distinguish between imaging in the conventional mode (quasi-parallel illumination) and in the scanning mode (using a focused electron probe), as well as between diffraction contrast at low/medium resolutions and phase contrast in high-resolution imaging.

In SEM, the contrast mechanisms are divided into those preferentially obtained by imaging secondary electrons (with energies <50 eV, i.e., topography and doping contrast^{16,17} and those acquired by imaging backscattered electrons (having energies between 50 eV and the energy of the primary electron beam), i.e., compositional¹⁸ and channeling contrast.¹⁹ Good overviews on SEM imaging can be found in Refs. 16, 18, and 20.

2. Energy-dispersive x-ray spectroscopy (EDX)

This technique is a standard method in SEM and TEM to determine elemental and phase distributions in various material systems (the reader is referred to Refs. 18 and 21 for overviews on this method). While the spatial resolution in (scanning) TEM-EDX can be of the order of <0.1 nm,²² it can be as low as 10–20 nm for SEM-EDX.²³ Essential for achieving high spatial resolutions in SEM-EDX elemental-distribution maps is the use of small beam energies (few keV) and low-energy x-ray lines (i.e., on the order of 100 eV or smaller). Such lines exhibit small, inelastic mean-free paths, and, thus, the information volume (i.e., the effective volume in the analyzed material from which characteristic x rays are emitted and reach the EDX detector) is rather small, eventually leading to high spatial resolutions. As a consequence, the spatial resolutions in EDX elemental-distribution maps are different for different x-ray lines.

3. Electron backscatter diffraction (EBSD)

The basics of the EBSD technique are explained well in Refs. 24 and 25. By acquiring and evaluating electron backscatter diffraction patterns in each pixel of an area of interest, the

technique provides insight into sizes and orientations of grains in a polycrystalline material. From these data, grain-size distributions and texture information can be extracted. Moreover, it is possible to classify the grain boundaries between neighboring grains via their symmetry (misorientation), determine microstrain within individual grains,²⁶ and visualize and quantify dislocation densities.²⁷ The spatial resolution of EBSD analyses ranges from about 10 to 100 nm (orders of magnitude).

4. Cathodoluminescence (CL)

This method detects radiative recombination from a semiconductor (or insulator) as luminescence emission, induced by an incident electron beam. Good overviews on this technique can be found in Refs. 28 and 29. Hyperspectral CL maps (i.e., acquiring a CL spectrum per pixel) provide information with spatial resolutions of the order of 10–100 nm about phase distributions via the emission energies (can be compared with the elemental or phase distributions from EDX analyses), can be applied to trace dopants, and are a means to detect line or planar defects and assess recombination velocities at grain boundaries in a polycrystal (via decreases in the CL intensity at these defects).³⁰ For sufficiently slow processes, CL also allows for monitoring phase separation processes, as described in Sec. III B of the present work.

5. Electron-beam-induced current (EBIC) measurements

Overviews on EBIC analyses performed on semiconductor devices are provided by Refs. 2 and 31. Basically, this technique measures the current collected at the contacts of a semiconductor device (such as a solar cell or a light-emitting diode) upon local generation of charge carriers (electron–hole pairs). For devices with *p-n* junctions, it is possible to determine the width of the space–charge region and to estimate the diffusion length in the quasi-neutral region. For *p-i-n* or *n-i-p* junctions, for which the space–charge region extends across the entire absorber, the drift length of electrons and holes can be extracted. For the assessment of any material or device parameter, EBIC signals must be simulated using appropriate models.²

It is essential to vary the beam energy in order to investigate the effects of recombination of generated charge carriers at the analyzed surface and also the beam current to check for low-injection vs high-injection conditions. It is also possible, when using a lock-in amplifier in connection with an electron-beam blander, to apply a bias voltage to the device while performing the EBIC measurement, which allows for analyzing collection under various operation conditions.³²

D. Structure–property relationships from various analysis geometries

1. Plan/top view

The plan-view investigation of thin films or nanoparticles is the quickest and easiest way of electron microscopy analyses, since the effort for sample preparation is small. Figure 3 depicts various results obtained via SEM techniques from a halide-perovskite-type (HaP) thin film [i.e., fabricated by adding 5 mol. % MAPbCl₃ to a double-halide perovskite (C_{S_{0.22}FA_{0.78})Pb(I_{0.85}Br_{0.15})₃]. Since this}

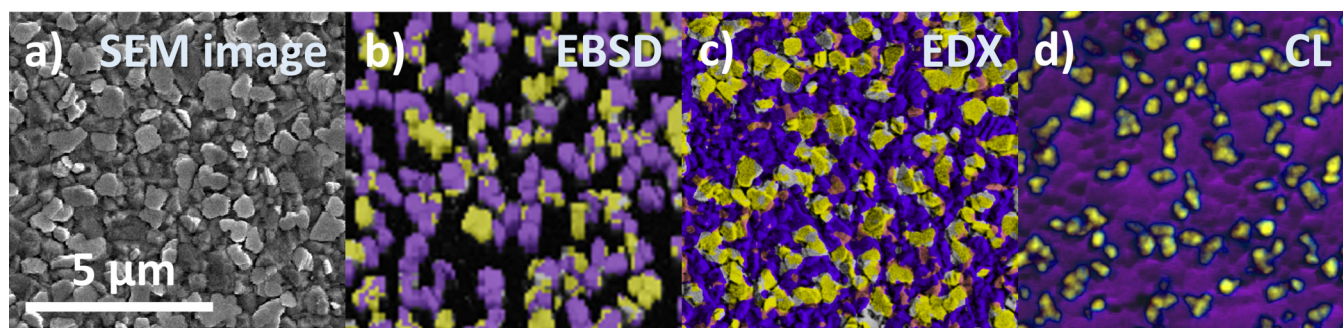


FIG. 3. Correlative electron microscopy at the example of a triple-cation metal-halide perovskite-type (HaP) film. (a) SEM image as well as composite images acquired by (b) EBSD, (c) EDX, and (d) CL. The HaP phase is highlighted by purple color, the PbI_2 precipitates by yellow color in (b)–(d).

material is sensitive to electron-beam irradiation, it was not possible to acquire the data on the identical specimen position. The SEM image [Fig. 3(a), acquired at 2 keV and about 10 pA] indicates a polycrystalline thin film with average grain sizes of a few 100 nm. From the EBSD phase-distribution map [Fig. 3(b), acquired at 28 keV and about 40 pA], PbI_2 precipitates inside or on top of the HaP film were detected. The presence of PbI_2 precipitates was confirmed (at 2–3.5 keV and about 40 pA) by means of (superimposed) EDX elemental-distribution maps [using N-K, purple, and I-M, yellow, x-ray lines, see Fig. 3(c)]. A CL map from the HaP film [Fig. 3(d)] again confirmed the EBSD and EDX results. For beam-sensitive materials such as HaP, hyperspectral maps can often not be acquired without considerable beam damage; instead, CL images are acquired at specific emission energies using band-pass filters. For phase analysis, these emission energies should correspond to the bandgap energies of the phases. The CL result depicted in Fig. 3(d) is composed of two monochromatic CL images recorded at (750 ± 50) nm (HaP, purple) and at (500 ± 50) nm (PbI_2 , yellow). By means of CL analyses on fractured cross sections (not shown here), it was verified that indeed, the PbI_2 precipitates resided on the HaP film surface. For more information on this study, the reader is referred to Ref. 33.

2. Back surfaces

For some thin-film device structures, it is useful to investigate both surfaces of a functional thin film. While one of these surfaces can be analyzed easily as described in Sec. II D 1, the other needs to be exposed by peeling off this functional thin film from another layer or from the substrate. One example for such a back-surface analysis is given in Figs. 4 and 5, which depict the characterization of a $\text{Cu}(\text{In,Ga})\text{Se}_2$ (CIGS)/ $\text{CdS}/\text{ZnO}/\text{ZnO}:\text{Al}$ stack. Exposing the CIGS back surface in this layer stack is facilitated by a very thin MoSe_2 film forming during the CIGS deposition on the Mo back contact, leading to mechanical instability of the CIGS/ MoSe_2 / Mo interface region and allowing for an easy lift off the Mo/glass substrate (Fig. 4). On the identical area of an exposed CIGS surface, EBSD, CL, and EBIC measurements were conducted (Fig. 5). Thus, it was possible to locate and classify grain boundaries (EBSD) and to correlate their crystallographic, their electrical (EBIC), and their

optoelectronic properties (CL).³⁵ Moreover, it was verified that there is no relationship between the local grain orientation and the corresponding charge-carrier collection and luminescence emission in the same grain.

3. Cross sections

Cross-sectional analyses of a thin-film solar cell provide direct access to the surface across which currents flow in the device (perpendicular to the substrate). Thus, for the microscopic characterization of thin-film devices, this configuration is of particular interest. Combining imaging as well as EBSD and EBIC analyses on an identical specimen area (Fig. 6) allows for correlating the microstructural properties of CIGS absorber layers in a $\text{ZnO}:\text{Al}/\text{ZnO}/\text{CdS}/\text{CIGS}/\text{Mo}/\text{glass}$ stack with the local collection properties.

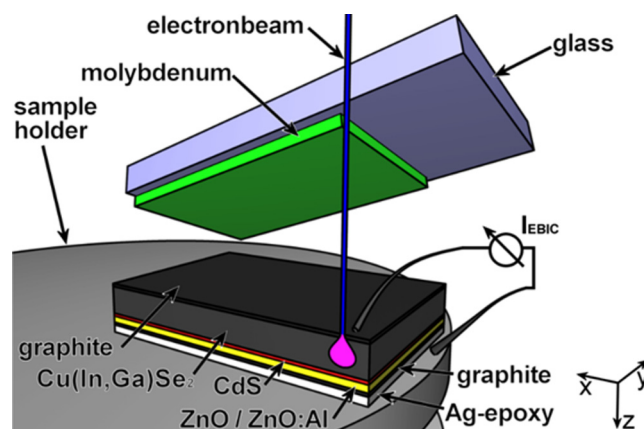


FIG. 4. Schematic drawing of lifting-off the glass/Mo substrate to access the back surface of CIGS/ $\text{CdS}/\text{ZnO}/\text{ZnO}:\text{Al}$ stacks. The graphite layer between the Ag epoxy and the $\text{ZnO}:\text{Al}$ layer inhibits Ag diffusion from the epoxy glue into the CIGS layer, while the graphite on top of the CIGS layer preserves the film surface and reduces drift during the SEM analyses. Reproduced with permission from Kavalakatt *et al.*, *J. Appl. Phys.* **115**, 014504 (2014). Copyright 2014 AIP Publishing LLC.³⁴

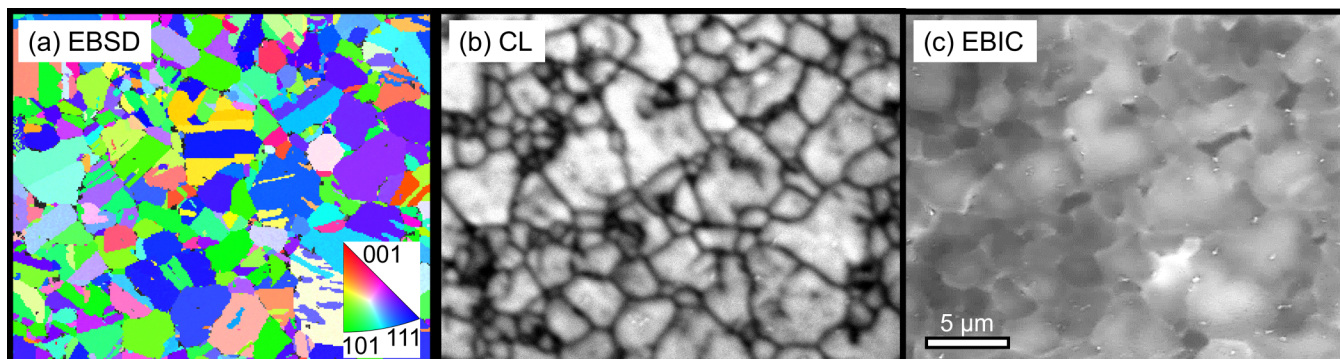


FIG. 5. (a) EBSD orientation-distribution map, (b) CL intensity distribution, and (c) EBIC image, all acquired on the identical CIGS back surface of a CIGS/CdS/ZnO/ZnO:Al stack. Adapted from Abou-Ras *et al.*, *Acta Mater.* **118**, 244 (2016).³⁵

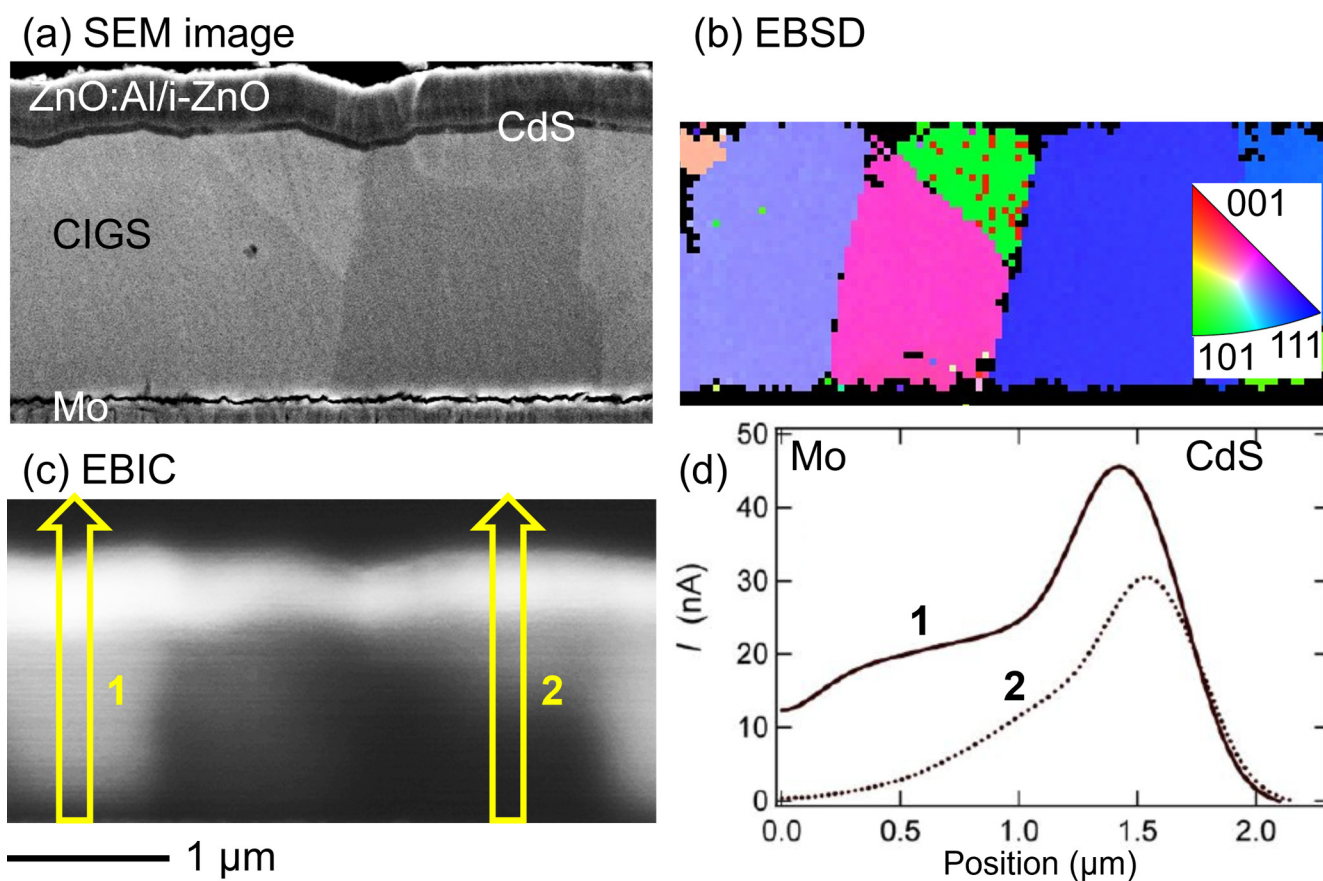


FIG. 6. (a) SEM image, (b) EBSD orientation-distribution map (local orientations provided by false colors, see legend), and (c) EBIC image from the identical area on a cross section of a solar cell with ZnO:Al/ZnO/CdS/CIGS/Mo/glass stack. Along the two arrows labeled by 1 and 2 in (c), linescans were extracted from the EBIC image (d). Adapted from Nichterwitz *et al.*, *Thin Solid Films* **517**, 2554 (2009).³⁶

Apparently, the width of the space-charge region [in Fig. 6(c), where the collection probability and, thus, the EBIC is largest due to the electrical field present] vary substantially along the p - n junction between the CIGS and the CdS layers. This variation can be explained by locally varying (charged) point defects, leading to spatially slightly varying net-doping densities in the CIGS, CdS, and ZnO:Al/i-ZnO layers as well as at the varying charge densities at the CIGS/CdS interface, resulting in corresponding fluctuations in the width of the space-charge region along the p - n junction. A recent work³⁷ indicated that indeed, lateral variations of interface charge densities have a particular impact on electrostatic potential fluctuations at the CIGS/CdS interface, visible via the variations in the width of the space-charge region in the EBIC images.

Moreover, also the EBIC signals in the quasi-neutral region [from the lower edge of the space-charge region, Fig. 6(c), to the Mo back contact] differ from grain to grain. This feature can be understood in terms of again locally varying (charged) point defects, leading to spatial variations of the lifetimes (of minority charge carriers, i.e., electrons in p -CIGS) and, thus, different decays of the EBIC signals [visible when comparing the profiles 1 and 2 in Fig. 6(d)]. No direct correlation between the grain orientations and the corresponding EBIC signals was found (see also Ref. 36).

Microstructural analyses by means of EBSD on cross-sectional specimens can be combined also with EDX and CL measurements on the identical areas. An example of such a correlative electron microscopy study is provided in Fig. 7. A correlation of the microstructure in the CIGS layers [Fig. 7(b)] with the elemental [Fig. 7(c)] or CL emission distributions [Fig. 7(d)] was not found. The Ga-distribution map [Fig. 7(c)] exhibits a Ga gradient present

in the CIGS perpendicular to the substrate. This compositional gradient affects the luminescence emission depicted in the CL map [Fig. 7(d)]. Indeed, also the CL emission energy features a gradient perpendicular to the substrate [Fig. 7(e)]. Since CIGS is a solid solution of CuInSe₂ and CuGaSe₂, and considering that these ternary compounds have different bandgap energies of 1.04 and 1.68 eV,³⁸ the local bandgap energy E_{gap} can be calculated using the compositional ratio $x = [\text{Ga}]/([\text{In}] + [\text{Ga}])$ via³⁹

$$E_{\text{gap}}(x) = (1 - x)E_{\text{gap}}(\text{CuInSe}_2) + xE_{\text{gap}}(\text{CuGaSe}_2) - bx(1 - x), \quad (1)$$

where b is the bowing factor ($b = 0.2$) and x is calculated from the EDX results. It is visible that the CL emission energies are smaller than the E_{gap} values by several 10 meV. This behavior is due to the broadening of the bandgap distribution induced mainly by the compositional/ E_{gap} gradient, leading to a decrease in the CL emission energy.^{40–42}

As visible in Fig. 7(d), the CL intensity is decreased at the position of randomly oriented grain boundaries [those not highlighted by yellow lines in Fig. 7(b)], which is owing to enhanced nonradiative recombination at these planar defects. By extraction of CL linescans across grain boundaries and applying a model proposed by Mendis *et al.*,³⁰ it is possible to estimate the recombination velocities at these grain boundaries. Such microscopic material parameters can be used as an important input for two-dimensional device simulations,⁴³ demonstrating the effect of grain boundaries in the polycrystalline absorber layer on the solar-cell performance.

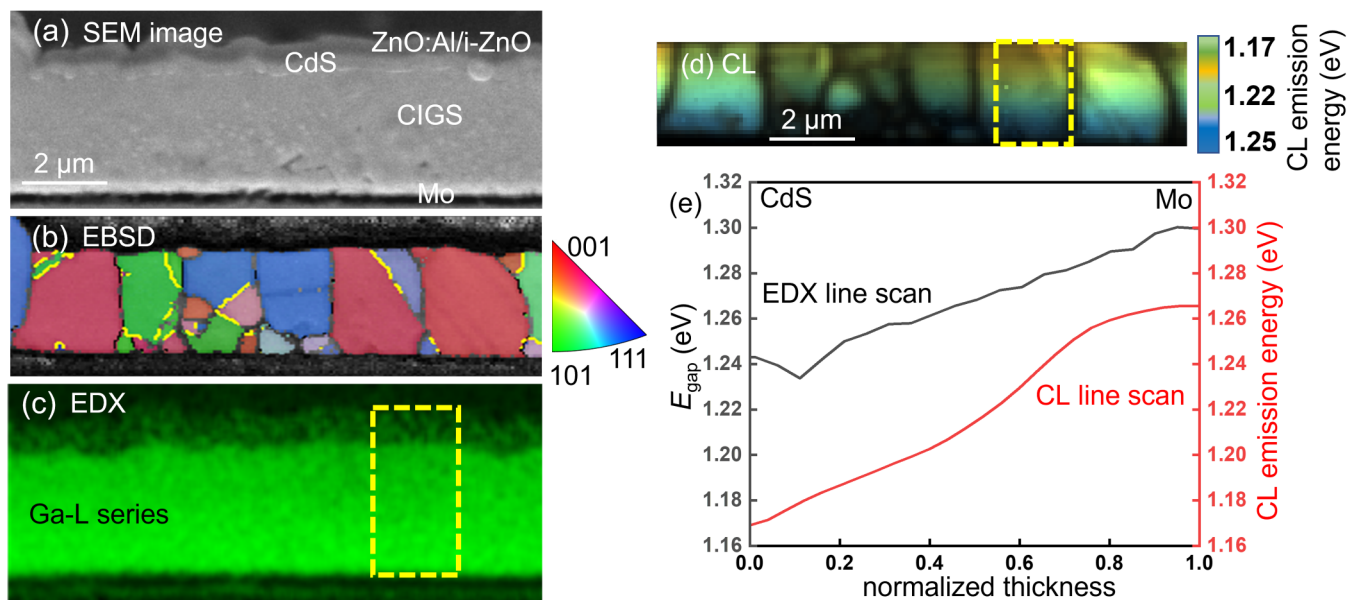
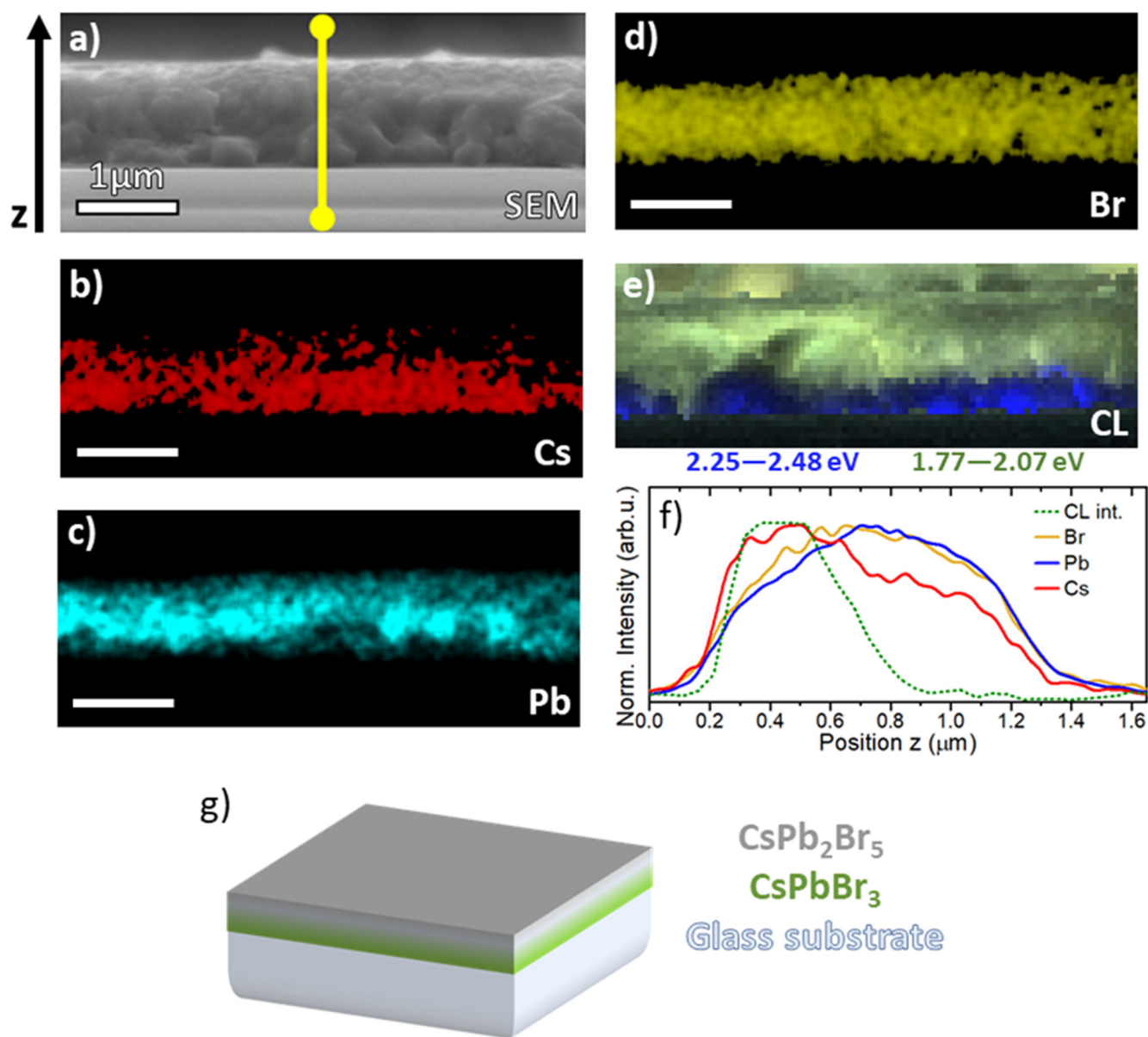


FIG. 7. (a) SEM image, (b) EBSD orientation-distribution map with twin boundaries highlighted by yellow lines, (c) Ga-distribution map obtained via EDX, and (d) CL emission distribution, all obtained on the identical area on a cross section of a solar cell with ZnO:Al/ZnO/CdS/CIGS/Mo/glass stack. Along the rectangles in (c) and (d), linescans were extracted from the Ga-distribution map and the CL image (e). The local bandgap energy in the CIGS layer was calculated using Eq. (1).

Cross-sectional analysis of HaPs materials poses a greater challenge in SEM, due to their inherited instability, water solubility (which prohibits their cross-sectional preparation as described in Sec. II B 1), and beam sensitivity. However, cleanly cleaved cross-

sectional surfaces can be analyzed and their compositional and optoelectronic properties across the cross section can be correlated, by using EDX and CL. For example, Fig. 8 shows the correlative microscopic analysis of a cleaved Cs–Pb–Br thin film on a glass



Downloaded from http://pubs.aip.org/aip/jap/article-pdf/doi/10.1063/5.0138952/1678727/121101_1_online.pdf

FIG. 8. Correlative SEM characterization of the cross section of a Cs–Pb–Br thin film on glass. (a) SEM image of this cross section and (b)–(d) corresponding EDX elemental-distribution maps using the Br-L, Cs-M, and Pb-M x-ray lines. (e) CL intensity maps, showing the luminescence from two energy intervals (2.25–2.48 and 1.77–2.07 eV) corresponding to the bandgap energies of CsPbBr₃ and CsPb₂Br₅. CL and EDX maps were acquired on the identical area. (f) The line scans extracted from the EDX and CL data along the yellow line in (a) show how the decrease in Cs content is correlated with the decrease in the CL intensity of the high-energy band. This correlative approach allows for identifying the layer stack containing the different phases of Cs–Pb–Br, CsPbBr₃, and CsPb₂Br₅, as well as their distributions on the glass substrate, as schematically shown in (g). Adapted from Caicedo-Dávila *et al.*, *J. Phys. Chem. C* **124**, 19514 (2020).⁴⁴

substrate. The plan-view measurements [not shown here, but the reader is referred to Ref. 44] show a large-grain film, which only exhibits luminescence at the grain boundaries. The cross-sectional EDX elemental-distribution maps [Figs. 8(b)–8(d)] reveal that the Cs counts are depleted toward the surface of the film, while the Pb counts follow the opposite trend [Fig. 8(f), solid lines]. The changes in the composition correlate with the CL intensity in the visible range of the spectrum (~ 2.35 eV) measured on the exact same area. Such emission is intense close to the substrate but completely quenched toward the substrate [Fig. 8(f), dotted line]. Two phases are identified across the film. EDX quantitative analysis of the relative composition of the phases revealed that the HaP CsPbBr₃, emitting at 2.35 eV forms near the substrate, while the wide-gap CsPb₂Br₅ forms at the surface. This clarifies that the emission at the grain boundaries stems from the bottom phase, owing to deeper penetration of the electron beam. Furthermore, combining this correlative approach with macroscopic spectroscopic and structural characterization can lead to a deeper understanding of phase transformation and their effect on recombination and optoelectronic properties of the material (see Ref. 44 for further information).

4. Combinations of electron microscopy with scanning-probe and light microscopy techniques

It is noteworthy that apart from combining various SEM techniques on the identical specimen areas, as demonstrated in Sec. II D, SEM methods can also be correlated with scanning-probe and light microscopy techniques. The following subsections will give an overview of corresponding analyses:

a. Raman microspectroscopy combined with EBSD. Raman spectroscopy is an established technique for the analysis of structural and compositional material properties. Indeed, when analyzing crystalline specimens, Raman intensities are dependent on the local crystal orientation.⁴⁵ Thus, Raman microspectroscopy (acquiring a series of Raman spectra while scanning across a specimen area) provides the means to obtain local orientations on polycrystalline materials with lateral resolutions at the submicrometer level. By the acquisition of EBSD maps on the same identical specimen positions, these local crystal orientations can be confirmed.⁴⁶ Moreover, the local orientation information obtained by means of EBSD can be used to calculate the theoretical Raman intensities for specific grain orientations, using the approaches provided by Refs. 47 and 48.

b. Scanning Kelvin-probe force microscopy combined with EBSD. Scanning Kelvin-probe force microscopy (SKPFM) is a scanning-probe technique that gives a means to determine the local differences in the work function at the surfaces of thin films via the lateral distributions of the contact-potential difference. When moving from the grain interiors to grain boundaries in polycrystalline, semiconductor thin films, the work function can be expected to change owing to the presence of band bending at the grain boundaries. This upward or downward band bending is the result of excess-charge densities at the grain-boundary planes, which are screened by the free charge carriers in the semiconductor, leading

to a change in the electrostatic potential corresponding to Poisson's equation. When combined with EBSD analyses on the identical specimen areas, it is possible to identify and classify grain boundaries according to their symmetries and eventually correlate the grain-boundary symmetry with the band bending determined by SKPFM.^{49,50}

c. Scanning tunneling microscopy and spectroscopy combined with EBSD. Scanning tunneling spectroscopy (STS) in the corresponding microscopy (STM) measures the current I between a sharp metal tip and the sample as a function of the applied bias voltage V . The local differential conductivity dI/dV is obtained, providing access to the density of states on the analyzed surface and, thus, to the electronic defect-level density within an energy range eV around the Fermi level at nm lateral resolution.⁵¹ Since the surfaces of polycrystalline thin films are prone to surface faceting, STM, STS, and EBSD can be combined on the identical specimen areas to correlate the electronic defect-level density with the crystal facets of grain surfaces on CuInSe₂ thin films. EBSD determined the local orientation of the grain (perpendicular to the substrate), STM provided the angles of the surface facets with respect to the substrate and thus, an estimate for the crystal planes at the faceted surface, while STS measured the electronic defect-level density on each facet. It became apparent that surface facets with high densities of defects are of polar nature, whereas passivated regions consisted of nonpolar crystal facets. Further information on this work can be found in Ref. 51.

d. Scanning spreading resistance microscopy combined with EBSD. Scanning spreading resistance microscopy (SSRM) is based on atomic force microscopy and probes the two-dimensional resistivity as well as the carrier distribution in semiconductor devices.⁵² When combining SSRM with EBSD, it is possible to determine the carrier distributions in each grain of a polycrystalline layer. Moreover, variations in resistivity across grain boundaries can be measured and correlated with the grain-boundary symmetry. According to Refs. 53 and 54, the net-doping densities in polycrystalline Cu(In,Ga)Se₂ thin films are not homogeneously distributed, but differ between neighboring grains and also within individual grains on the same order of magnitude. Moreover, high-symmetry (twin) boundaries did not exhibit a change in the SSRM signal, whereas at random grain boundaries, a measurable decrease in resistivity was measured, indicating upward band bending or electron barriers in the p -type Cu(In,Ga)Se₂.

e. Atom-probe tomography combined with TEM imaging, EBSD, and EBIC. Atom-probe tomography (APT) is a mass-spectroscopy technique with very high spatial resolution. When analyzing elemental distributions in polycrystalline semiconductor thin films, it is possible to extract elemental distributions at interfaces as well as at and around line and planar defects. An overview of the technique including also applications to thin-film solar cells can be found in Ref. 55. Correspondingly, the acquisition of an EBSD map on a sample allows for selecting the area of interest (e.g., a grain boundary with a specific misorientation). From this area, a needle-shaped specimen is cut out using FIB (Sec. II B 2). The diffraction contrast in TEM images as well as EBSD maps of

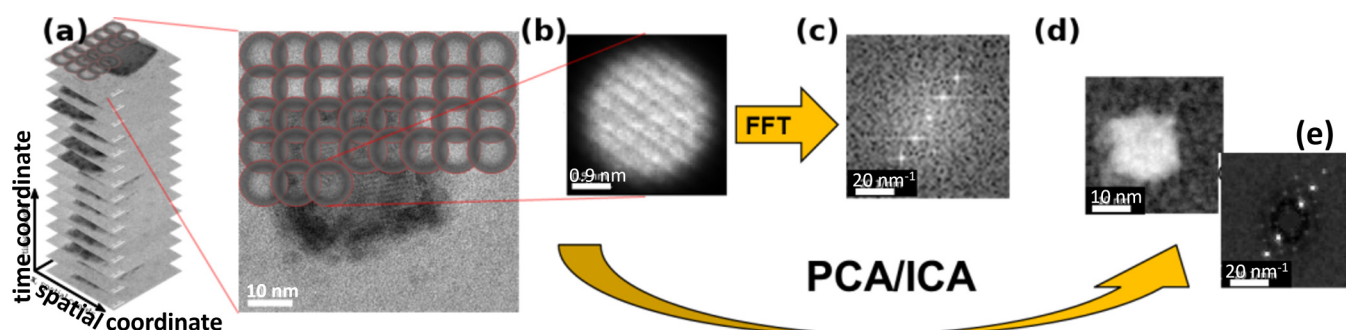


FIG. 9. (a) Initial image is virtually scanned, (b) individual patch, (c) FFT of patch, and (d) abundance map for (e) the corresponding diffractogram. Adapted from Funk *et al.*, Phys. Chem. Lett. 11, 4945 (2020).⁶¹

this specimen provides an overview of individual grains as well as of existing line and planar crystal defects. These TEM images are also an essential template for the three-dimensional reconstruction of the specimen from the stack of two-dimensional APT datasets. The elemental distributions in the APT data can be combined with the local short-circuit current via EBIC images acquired on the identical positions prior to the FIB preparation.⁵⁶

III. MONITORING OF PHASE SEGREGATION PROCESSES IN NANOPARTICLES AND THIN FILMS

In this section, we will give insight into possibilities to monitor phase segregation processes in nanoparticles and thin films by means of transmission and scanning electron microscopy techniques. We will demonstrate corresponding approaches at the example of mixed-halide perovskites, in which such phase segregation processes induced by various radiation sources occur frequently.

A. Multivariate analysis of time-series diffractogram datasets extracted from high-resolution transmission electron micrographs

1. Introduction

Diffractogram patterns are commonly used to assess crystallinity and aberrations from high-resolution transmission electron microscopy (HRTEM) images.^{57,58} Such patterns, typically calculated by fast Fourier transformation (FFT) of the image data, can be seen as a way to codify and present structural information. For instance, lattice spacing in a crystalline specimen is identified by characteristic spots in its diffractogram pattern.

We have designed a simple procedure that exploits the information in diffractogram patterns in order to analyze large amount of image data at once. In a nutshell, our algorithm first encodes structural information in a HRTEM image dataset and then uses multivariate analysis (MVA) to classify this information. Since the diffractogram dataset we create is conceptually similar to a scanning nano-beam electron diffraction (NBED) dataset, our approach can be thought as related to previous works that have applied unsupervised learning to study NBED datasets.^{59,60}

Our proposed workflow, as depicted in Fig. 9, is divided into two main sections, which are explained below in detail. The first one comprises pre-processing of a HRTEM image dataset into a diffractogram dataset, and the second one, applying unsupervised machine learning to detect structural features.

Such procedures have proven useful for processing and interpreting time-resolved HRTEM image series of inorganic mixed-halide perovskites.^{59,62} The resulting multivariate analysis (MVA) decomposition factors were related to different phases. The evolution of the abundance maps allowed for following the evolution of one CsPb(Br_{0.8}I_{0.2})₃ crystallite during its degradation under the electron beam. As depicted in Fig. 10, after 5 min of irradiation, the material changed completely as the iodine depleted from the core into the shell.

The complete time series in this example included images during 13 min, which are shown in Fig. 11(a). The entire results of our procedure are also included: the MVA factors in Fig. 11(b)

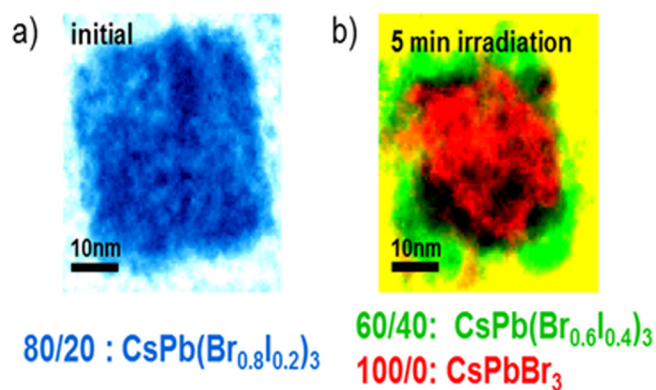


FIG. 10. Abundance maps given as false colors (a) for the phase in the initial state and (b) superposition of the phases present after 4 min of electron-beam exposure. While initially the particle consisted of single-phase CsPb(Br_{0.8}I_{0.2})₃, it was transformed to a mixture of CsPb(Br_{0.6}I_{0.4})₃ and CsPbBr₃ after 5 min of irradiation. Reproduced with permission from Funk *et al.*, J. Phys. Chem. Lett. 11, 4945 (2020). Copyright 2020 American Chemical Society.⁶¹

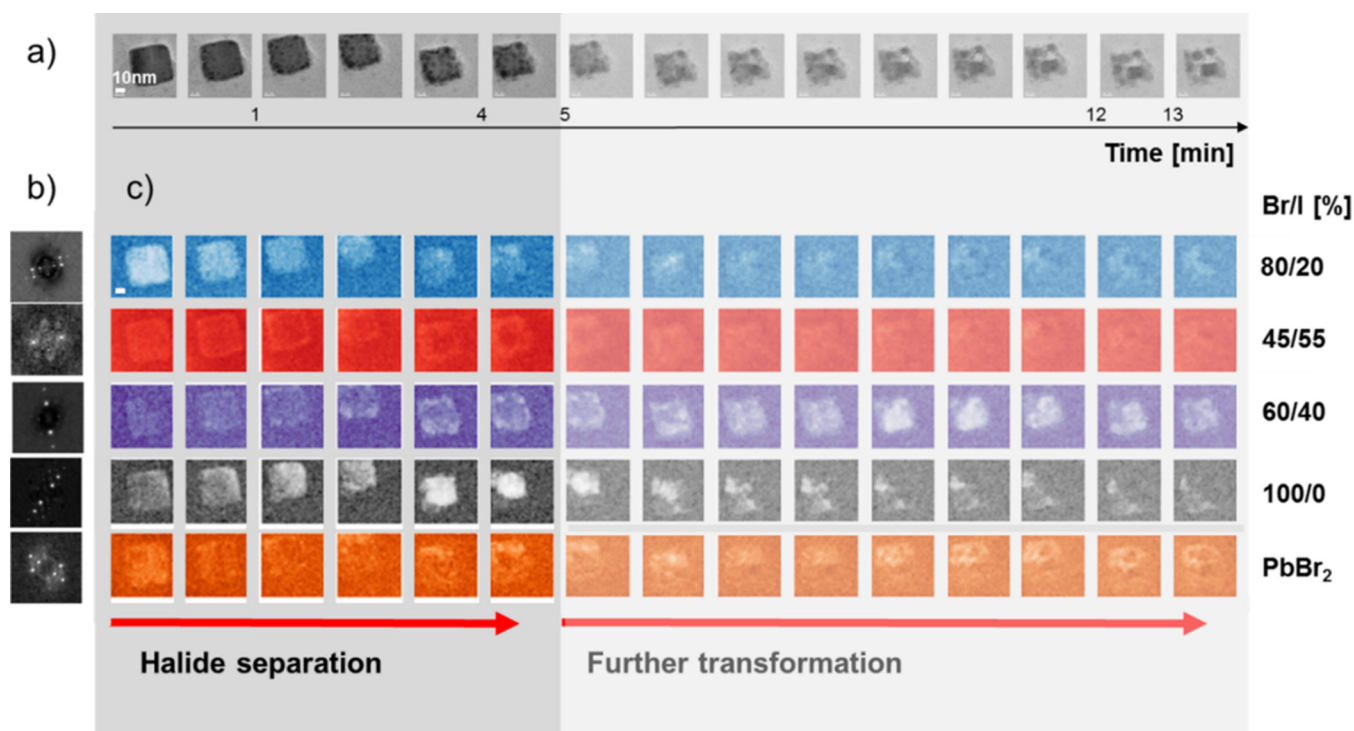


FIG. 11. (a) HRTEM images acquired during the 13 min of total acquisition duration while exposing the specimen continuously to (near-)parallel electron-beam irradiation, (b) characteristic diffraction patterns of the five abundant structures, (c) corresponding abundance maps identified as $\text{CsPb}(\text{Br}_{x1-x})_3$ for $x = 0.8, 0.45, 0.6, 1.0$, and also as PbBr_2 . High intensity in a pixel corresponds with a high abundance of the structure in this pixel. Reproduced with permission from Funk *et al.*, *J. Phys. Chem. Lett.* **11**, 4945 (2020). Copyright 2020 American Chemical Society.⁶¹

condense the structural information and typically look like noise-free diffractograms; meanwhile, the MVA loadings map the dynamically changing abundance of each phase [Fig. 11(c)].

2. Workflow

The pre-processing part of our workflow aims to extract diffractograms from overlapping regions, eliminating possible artifacts and obtaining homogeneous results. One example of such artifacts is dead and hot pixels that would introduce singularities in the calculations below. This relevant step might be modified depending on the experimental conditions (detector type, elevated noise levels).

Overlapping image patches are then extracted from the images as depicted in Fig. 9(a). This procedure is controlled by D_P and D_S the patch size and stride parameters as shown in detail in Fig. 12. The resulting image patches are of $D_P \times D_P$ size, with a separation between them of D_S . This procedure is repeated all over the image, taking into account that the patches need to fit inside of the image boundaries. From an image with spatial dimensions of size $N_{x,y}$, this procedure results in a diffractogram dataset with two “raster” dimensions with sizes $R_{x,y} = \text{floor}[(N_{x,y} - D_P)/D_S]$.

To give an example of typical parameters, we employed a patch size and stride of 64 and 8 pixels. 64×64 patches were

extracted that overlap for a total 56 pixels (see Fig. 12). For an image of size 1024×1024 pixel, we obtain a $120 \times 120 \times 64 \times 64$ image patch dataset, taking into account border effects. For each image patch a diffractogram is obtained, meaning these are also the dimensions of the diffractogram dataset.

Before obtaining diffractograms from these image patches, an apodization filter is applied to them as shown in Fig. 12(b). We generally apply a smooth decaying filter, such as the two-dimensional version of the Butterworth filter. The implementation is, as explained in Ref. 63, $B(r) = 1 / [1 + (r/r_B)^{N_B}]$, where r is the distance from the center of the image patch, while r_B and N_B are parameters controlling the cut-off and steepness of the filter. The effect of these parameters can be examined in Fig. 13.

The filter parameters are carefully chosen in order to allow the intensity at the border of the image patch to decay to zero. We additionally choose to subtract the mean intensity from each image patch, so the filter is applied as follows, $I_B = IB + \langle I \rangle (1 - B)$, where I and I_B are the image patches before and after filtering, and the chevrons denote averaging.

For each filtered image patch, a diffractogram is obtained as expressed in Fig. 9(c). The diffractograms are calculated from the spectral density of the pre-processed patches, $|\hat{I}_B| = |\text{FFT}(I_B)|$. In order to compress the dynamic range of the FFT result, we employ the following formula for the diffractogram, $D = 10\log_{10}(|\hat{I}_B|)$.

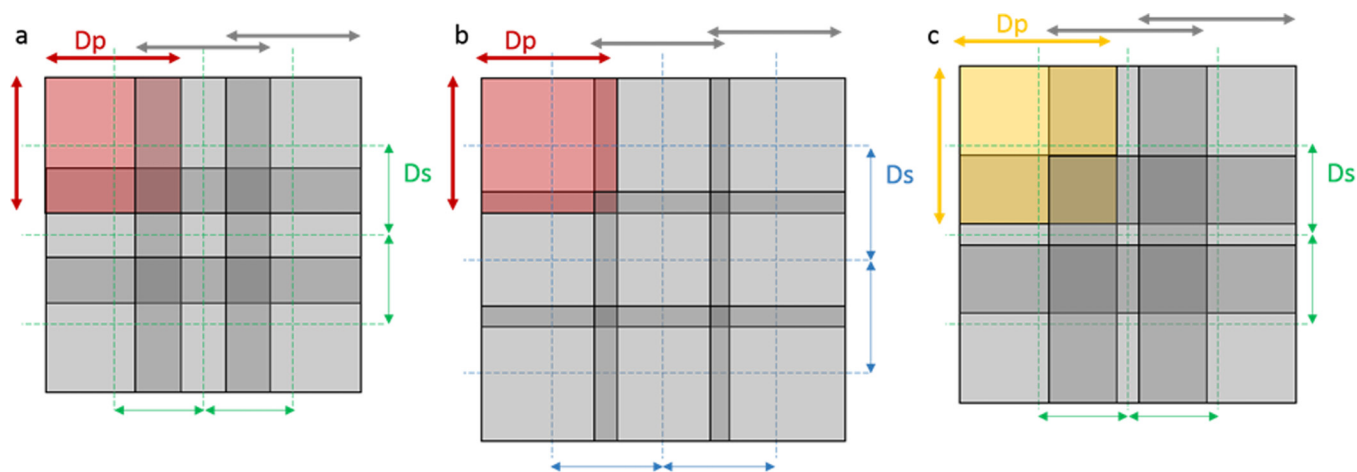


FIG. 12. Influence of patch size D_p and step size D_s . (a) shows a smaller step size compared with (b), while the patch size is kept constant for (a) and (b). (c) shows a larger patch size and a constant step size with respect to (a). The larger the patch size, the better the resolution of the FFT and also the larger the area from which it stems. The larger the step size, the smaller the resolution of the final abundance map.

After the pre-processing workflow, the diffractogram dataset is saved to disk to allow for the analysis part of the workflow to proceed. Even with compression, it is unfeasible to load and keep all the data at once in the computer random-access memory (RAM), considering that we aim to perform analysis of

diffractogram datasets for time series which are comprised of N_t images. In order to reduce the size in disk, we save these files using HDF5 compression as implemented in Hyperspy.⁶⁴ For those settings, a standard diffractogram dataset occupied ~ 170 megabytes in disk space, taking only $N_t > 6$ images to occupy 1 gigabytes.

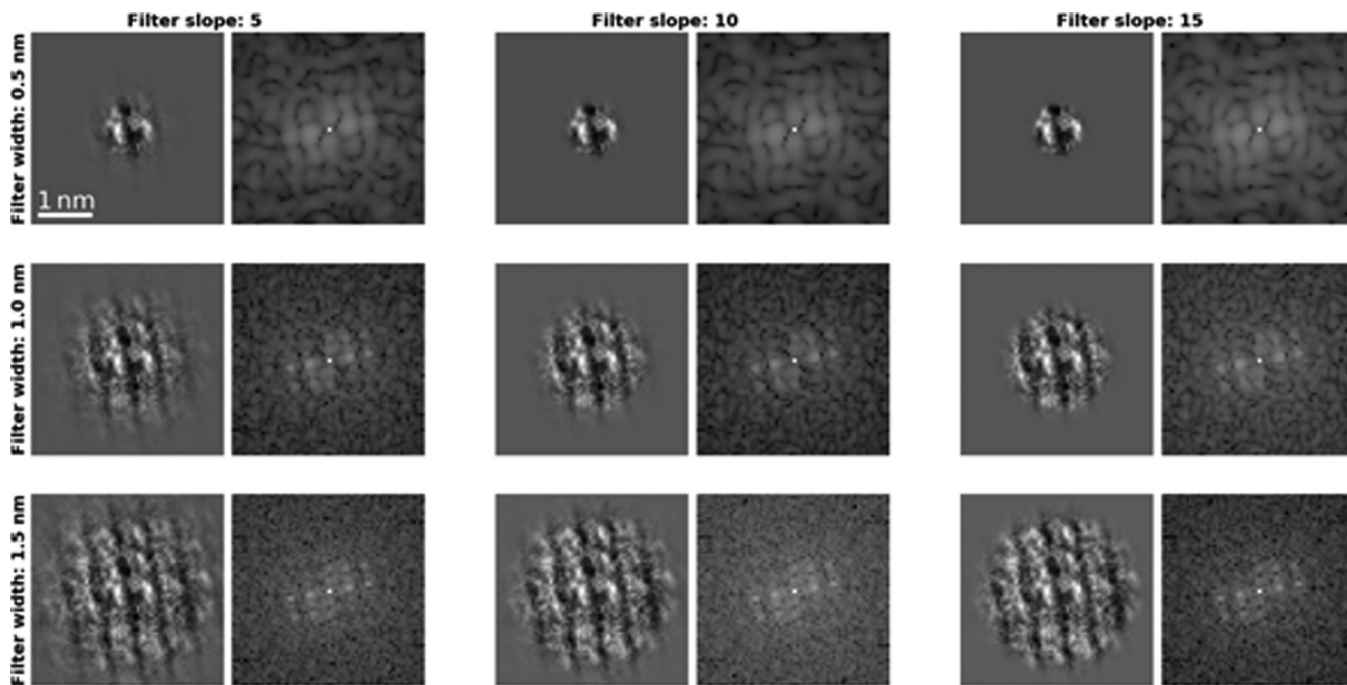


FIG. 13. Image patches and corresponding diffraction patterns for various filter widths r and filter slopes N_b .

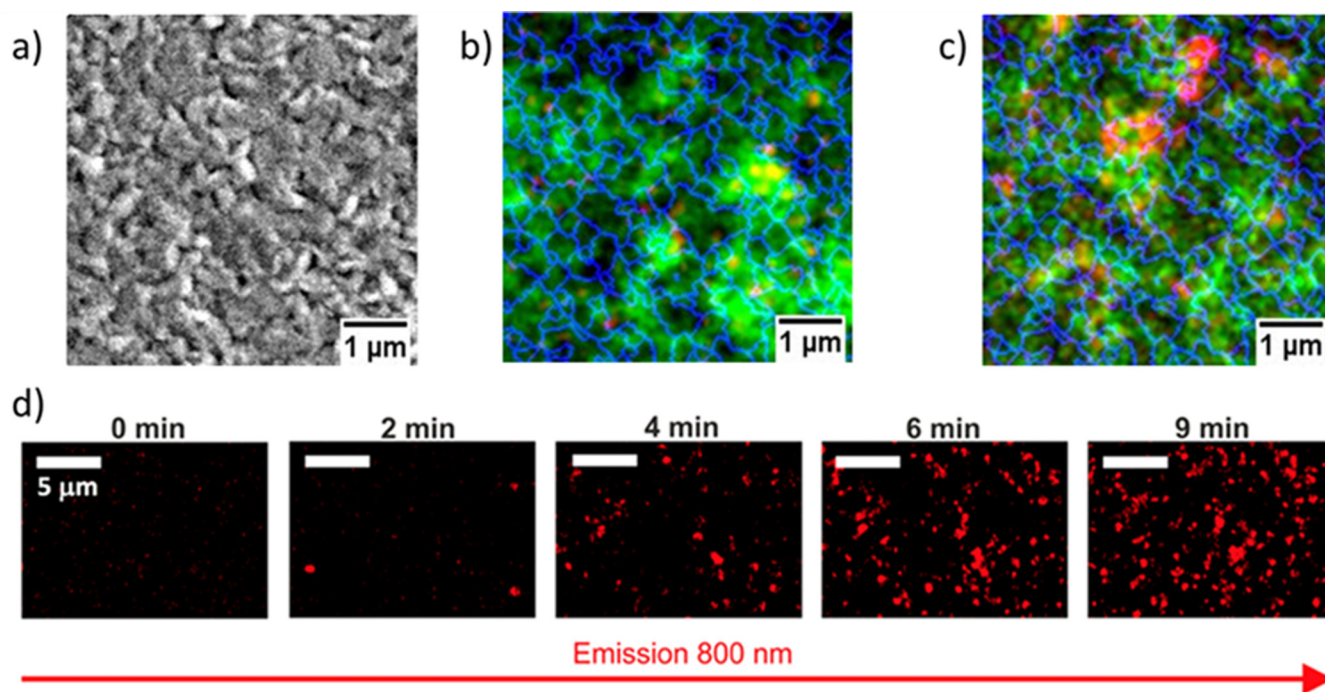


FIG. 14. CL *in situ* and *ex situ* investigation of phase segregation in triple-cation, double-halide perovskite. (a) SEM image of the surface of the film, and the corresponding CL intensity maps measured with a 700 (green) and 800 nm (red) bandpass filter before (b) and after (c) electron-beam-induced phase segregation. In (b) and (c), the grain boundaries extracted from the SEM image in (a) are highlighted by blue lines. (d) Snapshots of the 800 nm CL intensity map at different times under electron-beam illumination, showing the process of phase segregation. Adapted from Gutierrez-Partida *et al.*, ACS Energy Lett. **6**, 1045 (2021).⁶⁷

Once the diffractogram datasets are available, the workflow proceeds by applying unsupervised learning to reveal structural features, which is the last step in Fig. 9. Our implementation employs incremental MVA using online principal component analysis (PCA)⁶⁵ followed by blind source separation using the standard independent component analysis (ICA) algorithm (FastICA)⁶⁶ as implemented in Hyperspy.

The *online* prefix means that the PCA algorithm loads *chunks* of data in memory and performs for each one singular value decomposition (SVD). The most significant singular vectors are kept and used at the end to project the data to a lower dimensional space. Choosing an adequate *chunk* size allows to control the amount of memory occupied by the computations. This strategy allows us to keep manageable memory loads during this computation, theoretically allowing to process datasets of arbitrary size.

The PCA results are examined before carrying out ICA, in order to determine the number or representative components, M . The usual method of plotting the explained variance ratio (scree plot) and looking for the elbow threshold value is employed here. Additionally, the decomposition factors are individually assessed to look for structural features. The input of the ICA algorithm is the PCA result and the identified number of relevant components.

Finally, a MVA decomposition of the time-series diffractogram dataset in M components is obtained, such as $D = \sum_{i=0}^M F_i L_i$, where i runs through the components in order of relevance, F are

the decomposition factors that have diffractogram dimensions $D_P \times D_P$, as in Fig. 11(b), and L are score matrices with “raster” dimensions of size $N_t \times R_x \times R_y$, as in Fig. 11(c).

B. Combined SEM imaging and cathodoluminescence

Figure 14 shows the *ex situ* and *in situ* monitoring of the phase segregation process in a thin film of the double-cation, mixed-halide perovskite, $\text{Cs}_{0.18}\text{FA}_{0.82}\text{Pb}(\text{I}_{1-x}\text{Br}_x)_3$. A segmentation algorithm⁶⁸ that computes the watersheds in grayscale images was used to extract the apparent grain-boundary grid of the thin film from the SEM image in Fig. 14(a). Briefly, the algorithm detects the minima (below a threshold) of an inverted SEM image and simulates “flooding of water” from those minima by an iterative queue of pixels, generating basins, which correspond in our SEM images to the grains. Basins below a given size are disregarded. Finally, the segmented image is inverted to generate the grid with the apparent grain boundaries. This grid was superimposed on the CL maps in Figs. 14(b) and 14(c) (blue lines). Thus, the microstructure of the film was correlated with its emission properties at sub- μm resolution. The CL maps were acquired using two bandpass filters centered at 700 and 800 nm (50 nm band width), shown in green and red, respectively. Figure 14(b) depicts the CL maps of the film as deposited, which exhibits a dominant contribution of the 700-nm emission, corresponding to the expected wavelength for the

luminescence from the mixed-halide perovskite. The surface also exhibits small, localized 800-nm emission spots close to and at the grain boundaries. These small emitters are identified as iodine-rich perovskite phase, $\text{Cs}_{0.18}\text{FA}_{0.82}\text{PbI}_3$.

The CL map after phase segregation [Fig. 14(c)] induced by the exposure of the mixed-halide perovskite to the electron beam, with a controlled electron dose of below 2×10^{14} electrons/cm² that minimizes the effect of beam damage, shows that the area of the 800 nm emission phase increased considerably. Since the phase segregation is a slow process, the dynamics can be recorded in a series of CL intensity maps filtered at 800 nm, as shown in Fig. 14(d). These maps suggest that the phase segregation in the film starts from small isolated nano-emitting spots, nucleating all over the surface (at grain boundaries). The 800 nm emission after segregation is preferentially located at grain boundaries and areas where the intensity of the 700 nm emission was low in the fresh film. This suggests that defects facilitate the nucleation of the 800 nm nano-domains. Further details on this work can be found in Ref. 67.

IV. CONCLUSIONS

The present Tutorial provides a broad overview of the various means to apply correlative microscopy for the determination of microscopic structure–property relationships in optoelectronic semiconductor materials and devices. It was highlighted using examples from various studies that ideally, measurements should be conducted on the identical specimen areas for enhanced insights in materials properties and their correlations. Electron microscopy can also be well employed for the monitoring of phase segregation processes on various length scales ranging from sub-nm to micrometers. With the constantly increasing possibilities of using computer-based evaluation of correlative microscopy data, the extraction of materials and device properties can be expected to become much more effective, e.g., by applying machine learning or image registration, also on large microscopy datasets.

ACKNOWLEDGMENTS

The present work was supported by the Research Schools MatSEC and HyPerCells, the BMBF-funded project CATLAB, the BMWi/BMWK-funded projects EFFCIS and EFFCIS-II under Contract Nos. 0324076B and 03EE1059B, and the German-Israeli Helmholtz International Research School HI-SCORE (HIRS-0008). A.E. and C.T.K. acknowledge the German Research Foundation (DFG) for financial support via the Collaborative Research Center SFB 951.

AUTHOR DECLARATIONS

Conflict of Interests

The authors have no conflicts to disclose.

Author Contributions

Daniel Abou-Ras: Investigation (equal); Project administration (lead); Writing – original draft (lead). **Ulrike Bloeck:** Investigation (equal); Writing – original draft (equal). **Alberto Eljarrat:** Investigation (equal); Methodology (equal); Writing – original

draft (equal). **Hannah Funk:** Investigation (equal); Writing – original draft (equal). **Adnan Hammud:** Investigation (equal); Writing – original draft (equal). **Sinju Thomas:** Investigation (equal); Writing – original draft (equal). **Thomas Lunkenbein:** Writing – review & editing (equal). **Christoph T. Koch:** Supervision (equal); Writing – review & editing (equal).

DATA AVAILABILITY

The data that support the findings of this study are available from the corresponding author upon reasonable request.

REFERENCES

- 1J. Ayache, L. Beaunier, J. Boumendil, G. Ehret, and D. Laub, *Sample Preparation Handbook for Transmission Electron Microscopy: Techniques* (Springer Science & Business Media, 2010).
- 2D. Abou-Ras and T. Kirchartz, “Electron-beam-induced current measurements of thin-film solar cells,” *ACS Appl. Energy Mater.* **2**, 6127 (2019).
- 3L. Giannuzzi and F. A. Stevie, *Introduction to Focused Ion Beams: Instrumentation, Theory, Techniques and Practice* (Springer Science & Business Media, 2004).
- 4J. Mayer, L. C. Giannuzzi, T. Kamino, and J. Michael, “TEM sample preparation and FIB-induced damage,” *MRS Bull.* **32**, 400 (2007).
- 5M. Schaffer, B. Schaffer, and Q. Ramasse, “Sample preparation for atomic-resolution STEM at low voltages by FIB,” *Ultramicroscopy* **114**, 62 (2012).
- 6R. Wang, T. Huang, J. Xue, J. Tong, K. Zhu, and Y. Yang, “Prospects for metal halide perovskite-based tandem solar cells,” *Nat. Photonics* **15**, 411–425 (2021).
- 7Q. Jeangros, M. Duchamp, J. Werner, M. Kruth, R. E. Dunin-Borkowski, B. Niesen, C. Ballif, and A. Hessler-Wyser, “*In situ* TEM analysis of organic-inorganic metal-halide perovskite solar cells under electrical bias,” *Nano Lett.* **16**, 7013–7018 (2016).
- 8M. U. Rothmann, W. Li, Y. Zhu, A. Liu, Z. Ku, U. Bach, J. Etheridge, and Y.-B. Cheng, “Structural and chemical changes to $\text{CH}_3\text{NH}_3\text{PbI}_3$ induced by electron and gallium ion beams,” *Adv. Mater.* **30**, 1800629 (2018).
- 9T. W. Kim and S. Uchida, “Role of FIB and TEM in organo-halide perovskite solar cell observations,” *Hitachi Sci. Instrum. News* **13**, 4 (2019); available at https://www.hitachi-hightech.com/file/global/pdf/sinews/si_report/130201.pdf.
- 10Y. Lu, H. Wang, Y. Chen, Akriti, X. Hu, L. Dou, Q. Mi, Z. Ning, and Y. Yu, “Focused ion beam preparation of halide perovskite microscopy specimens: Evaluation of the beam induced damage,” *J. Phys.: Condens. Matter* **34**, 414004 (2022).
- 11F. U. Kosasih, G. Divitini, J. F. Orri, E. M. Tennyson, G. Kusch, R. A. Oliver, S. D. Stranks, and C. Ducati, “Optical emission from focused ion beam milled halide perovskite device cross-sections,” *Microsc. Res. Tech.* **85**, 2351 (2022).
- 12C. S. Sung; H. T. Lee, and J. S. Luo, “TEM sample preparation tricks for advanced DRAMs,” in *Conference Proceedings from the 41st International Symposium for Testing and Failure Analysis (EDFAS, 2015)*, pp. 318–322.
- 13D. Abou-Ras, B. Marsen, T. Rissom, F. Frost, H. Schulz, F. Bauer, V. Efimova, V. Hoffmann, and A. Eicke, “Enhancements in specimen preparation of Cu(In, Ga)(S,Se)₂ thin films,” *Micron* **43**, 470 (2012).
- 14D. Abou-Ras, M. Nichterwitz, M. J. Romero, and S. S. Schmidt, “Electron microscopy on thin films for solar cells,” in *Advanced Characterization Techniques for Thin Film Solar Cells*, edited by D. Abou-Ras, T. Kirchartz, and U. Rau (Wiley VCH, 2016), Vol. 1, pp. 371–420.
- 15C. B. Carter and D. B. Williams, *Transmission Electron Microscopy: Diffraction, Imaging, and Spectrometry* (Springer, 2016).
- 16J. Cazaux, “From the physics of secondary electron emission to image contrasts in scanning electron microscopy,” *J. Electron Microscop.* **61**, 261 (2012).
- 17C. P. Sealy, M. R. Castell, and P. R. Wilshaw, “Mechanism for secondary electron dopant contrast in the SEM,” *Microscopy* **49**, 311 (200).

- ¹⁸J. I. Goldstein, D. E. Newbury, J. R. Michael, N. W. Ritchie, J. H. J. Scott, and D. C. Joy, *Scanning Electron Microscopy and X-ray Microanalysis*, 4th ed. (Springer, 2017).
- ¹⁹S. Zaefferer and N. N. Elhami, "Theory and application of electron channelling contrast imaging under controlled diffraction conditions," *Acta Mater.* **75**, 20 (2014).
- ²⁰K. Shimizu and T. Mitani, *New Horizons of Applied Scanning Electron Microscopy* (Springer Science & Business Media, 2009), vol. 45.
- ²¹D. C. Bell and A. J. Garratt-Reed, *Energy Dispersive X-ray Analysis in the Electron Microscope* (Garland Science, 2003).
- ²²B. Goode, A. Carlsson, M. Bischoff, A. Mohammadi-Gheidari, G. Fallag, G. Schwind, C. Maunders, D. Muller, and L. Kourkoutis, "Sub-Ångstrom EDX mapping enabled by a high-brightness cold field emission source," *Microsc. Microanal.* **26**(Suppl 2), 1508 (2020).
- ²³Z. W. Liu, C. Sun, R. Gauvin, W. Wu, Y. Zeng, and H. Demers, "High spatial resolution EDS mapping of nanoparticles at low accelerating voltage," *J. Test. Eval.* **44**, 2285 (2016).
- ²⁴edited by, A. J. Schwartz, M. Kumar, and B. L. Adams, *Electron Backscatter Diffraction in Materials Science*, 2nd ed. (Springer, 2009).
- ²⁵See <https://www.ebsd.com/> for basic information on EBSD.
- ²⁶A. J. Wilkinson, T. B. Britton, J. Jiang, and P. S. Karamched, "A review of advances and challenges in EBSD strain mapping," *IOP Conf. Ser. Mater. Sci. Eng.* **55**, 012020 (2014).
- ²⁷J. Wheeler, S. Piazzolo, D. J. Prior, P. W. Trimby, and J. A. Tielke, "Using crystal lattice distortion data for geological investigations: The weighted Burgers vector method," *Authorea* (published online, 2022).
- ²⁸B. G. Yacobi and D. B. Holt, *Cathodoluminescence Microscopy of Inorganic Solids* (Springer Science & Business Media, 1990).
- ²⁹H. Guthrey and J. Moseley, "A review and perspective on cathodoluminescence analysis of halide perovskites," *Adv. Energy Mater.* **10**, 1903840 (2020).
- ³⁰B. G. Mendis, L. Bowen, and Q. Z. Jiang, "A contactless method for measuring the recombination velocity of an individual grain boundary in thin-film photovoltaics," *Appl. Phys. Lett.* **97**, 092112 (2010).
- ³¹edited by, D. B. Holt and D. C. Joy, *SEM Microcharacterization of Semiconductors* (Academic Press, 1989).
- ³²D. Abou-Ras, N. Schaefer, N. Baldaz, S. Brunken, and C. Boit, "Electron-beam-induced current measurements with applied bias provide insight to locally resolved acceptor concentrations at p-n junctions," *AIP Adv.* **5**, 077191 (2015).
- ³³D. R. Wargulski, K. Xu, H. Hempel, M. Flatken, S. Albrecht, and D. Abou-Ras, "Relationship between annealing temperature and the presence of PbI₂ platelets at the surfaces of triple-halide perovskite films," under consideration at ACS En. Lett. (2023).
- ³⁴J. Kavalakkatt, D. Abou-Ras, J. Haarstrich, C. Ronning, M. Nichterwitz, R. Caballero, T. Rissom, T. Unold, R. Scheer, and H. W. Schock, "Electron-beam-induced current at absorber back surfaces of Cu(In,Ga)Se₂ thin-film solar cells," *J. Appl. Phys.* **115**, 014504 (2014).
- ³⁵D. Abou-Ras, N. Schäfer, T. Rissom, M. N. Kelly, J. Haarstrich, C. Ronning, G. S. Rohrer, and A. D. Rollett, "Grain-boundary character distribution and correlations with electrical and optoelectronic properties of CuInSe₂ thin films," *Acta Mater.* **118**, 244 (2016).
- ³⁶M. Nichterwitz, D. Abou-Ras, K. Sakurai, J. Bundesmann, T. Unold, R. Scheer, and H. W. Schock, "Influence of grain boundaries on current collection in Cu(In,Ga)Se₂ thin-film solar cells," *Thin Solid Films* **517**, 2554 (2009).
- ³⁷A. Nikolaeva, M. Krause, N. Schäfer, W. Witte, D. Hariskos, T. Kodalle, C. A. Kaufmann, N. Barreau, J. A. Márquez, S. Levenco, T. Unold, and D. Abou-Ras, "Electrostatic potential fluctuations and light-soaking effects in Cu(In,Ga)Se₂ solar cells," *Prog. Photovoltaics: Res. Appl.* **28**, 919 (2020).
- ³⁸M. I. Alonso, K. Wakita, J. Pascual, M. Garriga, and N. Yamamoto, "Optical functions and electronic structure of CuInSe₂, CuGaSe₂, CuInS₂, and CuGaS₂," *Phys. Rev. B* **63**, 075203 (2001).
- ³⁹S. H. Wei, S. B. Zhang, and A. Zunger, "Effects of Ga addition to CuInSe₂ on its electronic, structural, and defect properties," *Appl. Phys. Lett.* **72**, 3199 (1998).
- ⁴⁰U. Rau and J. H. Werner, "Radiative efficiency limits of solar cells with lateral band-gap fluctuations," *Appl. Phys. Lett.* **84**, 3735 (2004).
- ⁴¹S. Thomas, T. Bertram, C. A. Kaufmann, T. Kodalle, J. A. Márquez Prieto, H. Hempel, L. Choubrac, W. Witte, D. Hariskos, R. Mainz, R. Carron, J. Keller, P. Reyes-Figueroa, R. Klenk, and D. Abou-Ras, "Effects of material properties of band-gap-graded Cu(In,Ga)Se₂ thin films on the onset of the quantum efficiency spectra of corresponding solar cells," *Prog. Photovoltaics: Res. Appl.* **30**, 1238 (2022).
- ⁴²S. Siebentritt, U. Rau, S. Gharabeiki, T. P. Weiss, A. Prot, T. Wang, D. Adeleye, M. Drahem, and A. Singh, "Photoluminescence assessment of materials for solar cell absorbers," *Faraday Discuss* **239**, 112–129 (2022).
- ⁴³M. Krause, A. Nikolaeva, M. Maiberg, P. Jackson, D. Hariskos, W. Witte, J. A. Márquez, S. Levenco, T. Unold, R. Scheer, and D. Abou-Ras, "Microscopic origins of performance losses in highly efficient Cu(In,Ga)Se₂ thin-film solar cells," *Nature Commun.* **11**, 4189 (2020).
- ⁴⁴S. Caicedo-Dávila, R. Gunder, J. A. Márquez, S. Levenco, K. Schwarzburg, T. Unold, and D. Abou-Ras, "Effect of post-deposition annealing on the luminescence of mixed-phase CsPb₂Br₃/CsPbBr₃ thin films," *J. Phys. Chem. C* **124**, 19514 (2020).
- ⁴⁵S. Bhagavantam, "Effect of crystal orientation on the Raman spectrum of calcite," *Proc. Ind. Acad. Soc. A.* **11**, 62–71 (1940).
- ⁴⁶T. Schmid, N. Schäfer, S. Levenco, T. Rissom, and D. Abou-Ras, "Orientation-distribution mapping of polycrystalline materials by Raman micro-spectroscopy," *Nat. Sci. Rep.* **5**, 18410-1-7 (2015).
- ⁴⁷R. Loudon, "The Raman effect in crystals," *Adv. Phys.* **13**, 423 (1964).
- ⁴⁸J. B. Hopkins and L. A. Farrow, "Raman microprobe determination of local crystal orientation," *J. Appl. Phys.* **59**, 1103 (1986).
- ⁴⁹R. Baier, D. Abou-Ras, T. Rissom, M. C. Lux-Steiner, and S. Sadewasser, "Symmetry-dependence of electronic grain boundary properties in polycrystalline CuInSe₂ thin films," *Appl. Phys. Lett.* **99**, 172102 (2011).
- ⁵⁰R. Baier, C. Leendertz, D. Abou-Ras, M. C. Lux-Steiner, and S. Sadewasser, "Properties of electronic potential barriers at grain boundaries in Cu(In,Ga)Se₂ thin films," *Sol. Energy Mater. Sol. Cells* **130**, 124–131 (2014).
- ⁵¹A. Elizabeth, H. Conradi, S. K. Sahoo, T. Kodalle, C. A. Kaufmann, T. D. Kühne, H. Mirhosseini, D. Abou-Ras, and H. Mönig, "Correlating facet orientation, defect-level density and dipole layer formation at the surface of polycrystalline CuInSe₂ thin films," *Acta Mater.* **200**, 463–470 (2020).
- ⁵²P. De Wolf, J. Snauwaert, T. Clarysse, W. Vandervorst, and L. Hellems, "Characterization of a point-contact on silicon using force microscopy-supported resistance measurements," *Appl. Phys. Lett.* **66**, 1530 (1995).
- ⁵³M. Kawamura, T. Yamada, N. Suyama, A. Yamada, and M. Konagai, "Grain boundary evaluation of Cu(In_{1-x}Gax)Se₂ solar cells," *Jpn. J. Appl. Phys.* **49**, 062301 (2010).
- ⁵⁴S. Oonishi, M. Kawamura, N. Takano, D. Hashimoto, A. Yamada, and M. Konagai, "Characterization of Cu(In,Ga)Se₂ grain boundary properties by electron- and tip-probe methods," *Thin Solid Films* **519**, 7347 (2011).
- ⁵⁵O. Cojocaru-Mirédin, T. Schwarz, P. P. Choi, M. Herbig, R. Wuerz, and D. Raabe, "Atom probe tomography studies on the Cu(In,Ga)Se₂ grain boundaries," *J. Vis. Exp.* **74**, e50376 (2013).
- ⁵⁶M. Raghuvanshi, R. Wuerz, and O. Cojocaru-Mirédin, "Interconnection between trait, structure, and composition of grain boundaries in Cu(In,Ga)Se₂ thin-film solar cells," *Adv. Funct. Mater.* **30**, 2001046 (2020).
- ⁵⁷J. Zemlin and F. Zemlin, "Diffraction patterns by mouse click," *Ultramicroscopy* **93**, 77 (2002).
- ⁵⁸J. Barthel and A. Thust, "Aberration measurement in HRTEM: Implementation and diagnostic use of numerical procedures for the highly precise recognition of diffraction patterns," *Ultramicroscopy* **111**, 27 (2010).
- ⁵⁹S. Schlitt, T. E. Gorelik, A. A. Stewart, E. Schomer, T. Raasch, and U. Kolb, *Acta Crystallogr. Sect. A: Found. Crystallogr.* **68**, 536 (2012).
- ⁶⁰B. H. Martineau, D. N. Johnstone, A. T. J. van Helvoort, P. A. Midgley, and A. S. Eggeman, "Unsupervised machine learning applied to scanning precession electron diffraction data," *Adv. Struct. Chem. Imaging* **5**, 3 (2019).
- ⁶¹H. Funk, O. Shargaieva, A. Eljarrat, E. L. Unger, C. T. Koch, and D. Abou-Ras, *J. Phys. Chem. Lett.* **11**, 4945 (2020).

- ⁶²H. Funk, “Microscopic insights into phases and their transformations in inorganic halide perovskites,” Doctoral thesis (TU Berlin, 2022).
- ⁶³A. Eljarrat, J. Müller, M. R. S. Huang, and C. T. Koch, “Multi-focus TIE algorithm including partial spatial coherence and overlapping filters,” *Opt. Express* **26**, 11819 (2018).
- ⁶⁴Hyperspy, release V1.7.3.
- ⁶⁵D. Ross, J. Lim, R. Lin, and M. Yang, “Incremental learning for robust visual tracking,” *Int. J. Compu. Vision* **77**, 125 (2008).
- ⁶⁶A. Hyvarinen and E. Oja, “Independent component analysis: Algorithms and applications,” *Neural Networks* **13**, 411 (2000).
- ⁶⁷P. Caprioglio, S. Caicedo-Dávila, T. C.-J. Yang, C. M. Wolff, F. Peña-Camargo, P. Fiala, B. Rech, C. Ballif, D. Abou-Ras, M. Stolterfoht, S. Albrecht, Q. Jeangros, and D. Neher, *ACS Energy Lett.* **6**, 419 (2021).
- ⁶⁸L. Vincent, L. Vincent, and P. Soille, *IEEE Trans. Pattern Anal. Mach. Intell.* **13**, 583 (1991).